International Journal of Heat and Mass Transfer 52 (2009) 4835–4850

Contents lists available at ScienceDirect

International Journal of Heat and Mass Transfer

journal homepage: www.elsevier.com/locate/ijhmt

Transient thermo-solutal convection of water near 4 °C with opposing gradients in a square cavity

Jung Bae Yoon [a], Jinho Lee [b,*], P. Kandaswamy [b]

[a] Graduate School of Mechanical Engineering, Yonsei University, Seoul 120-749, Republic of Korea
[b] School of Mechanical Engineering, Yonsei University, Seoul 120-749, Republic of Korea

ARTICLE INFO

Article history:
Received 3 October 2008
Received in revised form 6 May 2009
Accepted 25 May 2009

Keywords:
Thermo-solutal convection
Density maximum
Opposing gradient

ABSTRACT

A numerical study of two-dimensional thermo-solutal convection of water in a square cavity heated from below and salted from above for various value of Lewis number is conducted. The maximum density associated with water around 4 °C occurs inside the cavity, as the top wall is maintained at 0 °C while the bottom wall temperature varies in the range 8–12 °C. The maximum density region acts as an obstacle to prohibit convectional heat, mass, and momentum transfer. These effects are investigated numerically in the domain $-5 \times 10^2 < Ra_T < 2 \times 10^4$, $1 \times 10^5 < Ra_S < 8 \times 10^6$ and $L = 0.015$ m length of square cavity where Ra is the Rayleigh number of the fluid. The effect of Lewis number on the heat, mass, and momentum transfer is also systematically studied. For certain range of parameters, it is interesting to find that the flow pattern may change inversely from rolling (fluid particles raise along both vertical side walls and fall along the vertical center line) to plume motion (fluid particles raise along the vertical center line and fall along both side walls) as the bottom wall temperature and top wall concentration increase. Further increase in the value of Rayleigh number results in oscillating two cell flow structure in the cavity. It is found that there is a temporal maximum absolute value of average Nusselt and Sherwood number followed by a temporal minimum absolute value of average Nusselt and Sherwood number in a small time interval ($0 < t < 300$ s) and the steady state is reached after a certain time interval at the bottom wall. These time intervals are reduced with increasing Lewis number. Also, critical Grashof number which accounts for oscillatory heat and mass transfer with Lewis number is studied and it reveals that an increase in Lewis number results in slowing down oscillation and oscillation cycle becomes shorter with increasing species Grashof number.

1. Introduction

The problem of the natural convection induced by buoyancy-driven effects due to thermal and solutal gradients including nonlinear dependence of density near the maximum density region has received considerable attention in recent years. In such a process the thermal and solutal buoyancy forces either aid or oppose each other, depending on the range of temperature and concentration due to the nonlinear dependence of density on temperature and concentration. The presence of maximum density region adds hydraulic resistance and changes the hydrodynamics of the flow which causes change in heat and mass transfer. For this reason, complex flow patterns may form due to differences in the rate of heat and mass transfer, competition between thermal and solutal boundary layer development and density reversal in the mixing region.

In a study of natural convection in water, Goren [1] showed that the flow pattern can seriously be affected by the occurrence of density maximum associated with temperature around 4 °C in pure water and proposed the parabolic density–temperature relationship valid in the range from 0 to 8 °C. Goren [1] found that for water at 4 °C the convective velocities are reduced by about 1/8 and 1/80 times than those in water at 20 °C for temperature variations of 1 and 0.01 °C, respectively. Such effects arise from the slow variation of density as a function of temperature in the vicinity of the density maximum due to density inversion. Because of the nonlinear density–temperature dependence of water near 4 °C, the commonly used Boussinesq approximation is no longer applicable.

Several studies have been devoted to natural convection in water near 4 °C in various container geometries. The effect of a maximum density on transient natural convection in an enclosed rectangular cavity was investigated by Robillard and Vasseur [2,3]. They found that the convective heat transfer, the flow pattern and the temperature profile can be influenced greatly by the presence of a density maximum of the convective flow. Blake et al. [4]

* Corresponding author. Tel.: +82 2 2123 2816; fax: +82 2 2123 2159.
E-mail address: Jinholee@yonsei.ac.kr (J. Lee).

0017-9310/$ - see front matter © 2009 Elsevier Ltd. All rights reserved.
doi:10.1016/j.ijheatmasstransfer.2009.05.019

Nomenclature

A	coefficient of generalized discretization equation
C_p	specific heat (J/kg K)
C	concentration (kmol/m^3)
D	mass diffusivity (m^2/s)
d	mass diffusion coefficient, ρD (kg/ms)
g	gravitational acceleration (m/s^2)
Gr_S	solutal Grashof number, $\frac{g\beta_S \Delta C L^3}{\nu^2}$
Gr_T	thermal Grashof number, $\frac{g\beta_T \Delta T L^3}{\nu^2}$
h_S	mass transfer coefficient (kg/m^2 s)
h_T	convectional heat transfer coefficient (W/m^2 K)
k	thermal conductivity (W/m K)
L	length and height of square cavity (m)
Le	Lewis number, $\frac{\alpha}{D}$
Nu	Nusselt number, $\frac{h_T L}{k}$
p	pressure (Pa)
Pr	Prandtl number, $\frac{\nu}{\alpha}$
Ra_S	solutal Rayleigh number, $\frac{g\beta_S \Delta C L^3}{\nu D} = Gr_S Sc$
Ra_T	thermal Rayleigh number, $\frac{g\beta_T \Delta T L^3}{\nu \alpha} = Gr_T Pr$
S	source term of generalized discretization equation
Sc	Schmit number, $\frac{\nu}{D}$
Sh	Sherwood number, $\frac{h_S L}{d}$
T	temperature (°C)
t	time (s)
u	x-directional velocity (m/s)
v	y-directional velocity (m/s)
x, y	Cartesian coordinates (m)

Greek symbols

α	thermal diffusivity, $\frac{k}{\rho C_p}$ (m^2/s)
β_S	volumetric species expansion coefficient (m^3/kmol)
β_T	volumetric thermal expansion coefficient (1/K)
Φ	dependent variable of General coordinates
η	independent variables of General coordinates
μ	molecular viscosity (N s/m^2)
ρ	density (kg/m^3)
ν	kinematic viscosity (m^2/s)
ξ	independent variables of General coordinates

Subscripts

h	high value
i,j,k	tensor notation
l	low value
nbr	neighborhood grid points around center node
P	location of grid point that corresponds to center
ref	reference value for volumetric thermal expansion coefficient
S	solutal property
T	thermal property
$wall$	value at the boundary
0	reference value for density

conducted a numerical simulation of natural convection in a horizontal water layer heated from below using density–temperature relationship proposed by Goren [1] with several value of Rayleigh number and aspect ratio. They found that for certain range of the Rayleigh number and aspect ratio, the conduction dominant heat transfer mode is present showing a good agreement of the corresponding critical values recommended by linear stability analysis proposed by Chandrasekhar [5], Drazin and Reid [6].

The experimental and numerical studies of Lee et al. [7,8] on double diffusive natural convection showed that in an enclosure flow structure was divided into four distinct flow regimes depending on the buoyancy force ratios when temperature and concentration gradients were horizontal. About these phenomena, Lee and Hyun [9] explained the process of flow development in detail using numerical analysis.

Our objective in the present study is to document numerically the characteristics of unsteady flow pattern and rate of heat and mass transfer aligned for various values of Rayleigh and Lewis number in a square cavity heated from below and salted from above. This geometry is simple and of fundamental interest, as demonstrated by the literature devoted to the classical Benard problem where the Boussinesq approximation is applicable (Chandrasekhar [5], Drazin and Reid [6]). Furthermore, the onset of convection and oscillatory flow in a square cavity with maximum density effect has been investigated based on unsteady calculations. Transient numerical simulations of thermo-solutal convection based on the complete nonlinear density–temperature relation heated from below is yet to be studied. Hence in this study, we investigate the thermo-solutal convection of water around its density maximum temperature contained in a square cavity heated at the bottom and salted at the top.

2. Basic equations

We consider the two-dimensional square cavity filled with water as shown schematically in Fig. 1(A). The cavity is bounded from above and below by solid walls maintained at different wall temperature and concentration. The bottom wall temperature is higher than the temperature of the upper wall as would be the case of lake water trapped under a sheet of ice. Also the top wall concentration is higher than the concentration of the lower wall. The boundary temperatures are such that they surround the 4 °C temperature associated with the density maximum in pure water at atmospheric pressure. In this study, we assume that the flow is Newtonian and there is no generation of heat and chemical reaction. From the Fourier's law of heat conduction and the Fick's law of diffusion, the continuity, momentum, energy, and concentration equations in tensorial form are

$$\frac{\partial \rho}{\partial t} + \frac{\partial}{\partial x_j}(\rho u_j) = 0, \tag{1}$$

$$\frac{\partial}{\partial t}(\rho u_i) + \frac{\partial}{\partial x_j}(\rho u_j u_i) = \rho f_i - \frac{\partial p}{\partial x_i} + \frac{\partial}{\partial x_j}\left(\mu\left(\frac{\partial u_i}{\partial x_j} + \frac{\partial u_j}{\partial x_i}\right)\right), \tag{2}$$

$$\frac{\partial}{\partial t}(\rho C_p T) + \frac{\partial}{\partial x_j}(\rho u_j C_p T) = \frac{\partial}{\partial x_j}\left(k\frac{\partial T}{\partial x_j}\right) + \frac{\partial}{\partial x_j}\left(u_i \mu\left(\frac{\partial u_i}{\partial x_j} + \frac{\partial u_j}{\partial x_i}\right)\right), \tag{3}$$

$$\frac{\partial}{\partial t}(C) + \frac{\partial}{\partial x_j}(u_j C) = \frac{\partial}{\partial x_j}\left(D\frac{\partial C}{\partial x_j}\right). \tag{4}$$

In this study, all thermal properties of water are assumed constant except density. Because of its associated nonlinear density–temperature relationship in the vicinity of 4 °C, the commonly used linear density–temperature relationship is no longer applicable to predict the anomalous density–temperature behavior of water in the temperature range 0–12 °C and hence in this paper, the fourth order temperature–density relationship of Kandaswamy et al. [10] is used to predict more accurate physical movement as

$$\rho = \rho_0\left[1 - \sum_{i=1}^{4}(-1)^i \beta_i (T - T_0)^i + \beta_5 (C - C_0)\right], \tag{5}$$

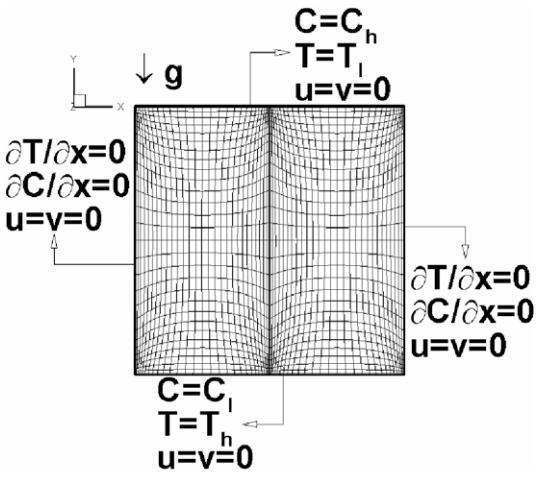

(A) Computational grid distribution

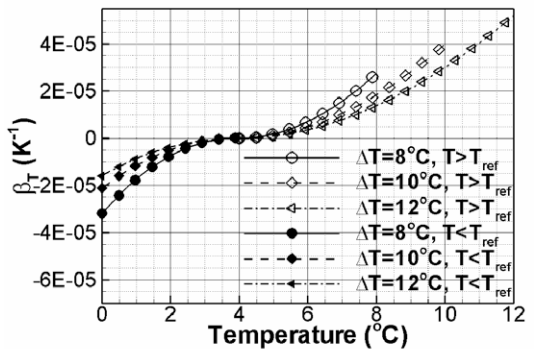

(B) Volumetric thermal expansion coefficient

Fig. 1. Schematic diagram for solution domain and computational grid distribution using 61×31 size with coordinate system and boundary conditions (A) and volumetric thermal expansion coefficient distributions for temperature difference, ΔT between top and bottom wall with internal temperature distributions, T according to reference temperature, $T_{ref} = 3.98$ °C (B).

where $\rho_0 = 999.845$ kg/m^3 is the density of water at $T_0 = 0$ °C, $C_0 = 0$ kmol/m^3 and $\beta_1 = 6.8143 \times 10^{-5}$ K^{-1}, $\beta_2 = 9.9901 \times 10^{-6}$ K^{-1}, $\beta_3 = 2.7217 \times 10^{-7}$ K^{-1}, $\beta_4 = 6.7252 \times 10^{-9}$ K^{-1}, and $\beta_5 = 3 \times 10^{-3}$ m^3/kmol. Because of fourth order relationship of density–temperature, in this study, the average value of volumetric thermal expansion coefficient is used to calculate Rayleigh number. If we equalize buoyancy force term based on nonlinear relationship of density–temperature without species transfer and linear relationship of Boussinesq approximation in y-directional momentum equation, average value of volumetric thermal expansion coefficient is defined as

$$\beta_T = \pm \frac{1}{\Delta T \rho_{ref} (T_{ref} - T_{wall})} \int (\rho - \rho_{ref}) dT, \tag{6}$$

where $\rho_{ref} = 999.973$ kg/m^3 at $T_{ref} = 3.98$ °C and in Eq. (6) positive sign represents compression region in the range $T_{wall} < 3.98$ °C and negative sign represents expansion region in the range $T_{wall} > 3.98$ °C. Also, ΔT is a positive value associated with boundary temperature. Fig. 1(B) is presented to show volumetric thermal expansion coefficient for temperature difference between top and bottom wall. From these profiles average values of volumetric thermal expansion coefficient are -3.8999×10^{-7} K^{-1}, 5.66858×10^{-6} K^{-1}, and 1.021994×10^{-5} K^{-1} that correspond to $T_{wall} = 8$ °C, 10 °C, and 12 °C.

The effect of fluid motion on the heat and mass transfer between two horizontal layers was evaluated by Nusselt and Sherwood numbers which are defined as

$$Nu = \frac{h_T L}{k} = \frac{1}{T_h - T_l} \int \frac{\partial T}{\partial y} dx, \tag{7}$$

$$Sh = \frac{h_S L}{d} = \frac{1}{C_h - C_l} \int \frac{\partial C}{\partial y} dx. \tag{8}$$

In this study, not to be defined values are assumed and material properties to be used in numerical calculation are $\mu = 1.514 \times 10^{-3}$ N s/m^2, $C_p = 4.202 \times 10^3$ J/kg K, $k = 5.7 \times 10^{-1}$ W/m K, and $d = 1.356 \times 10^{-5}$ kg/ms at $Le = 10$, $\beta_S = 3 \times 10^{-3}$ m^3/kmol, and $Pr = 11.16$. Thermal Rayleigh numbers are $Ra_T = -5.028 \times 10^2$, $Ra_T = 9.135 \times 10^3$, and $Ra_T = 1.976 \times 10^4$ associated with bottom wall temperature 8 °C, 10 °C, and 12 °C. Solutal Rayleigh numbers are $Ra_S = 1.257 \times 10^5$, $Ra_S = 2.563 \times 10^5$, and $Ra_S = 3.869 \times 10^5$ for top wall concentration 0.026 kmol/m^3, 0.053 kmol/m^3, and 0.08 kmol/m^3 at $Le = 10$.

In this study, we consider the region of calculation with same length of sides, $L = 0.015$ m and use no slip velocity boundary conditions at all four walls of the cavity. In order to calculate unsteady double diffusive natural convection, the initial conditions at $t < 0$ s are as

$$u = v = 0 \text{ m/s}, \quad T = T_l = 0\ ^\circ\text{C}, \quad C = C_l = 0 \text{ kmol/m}^3. \tag{9}$$

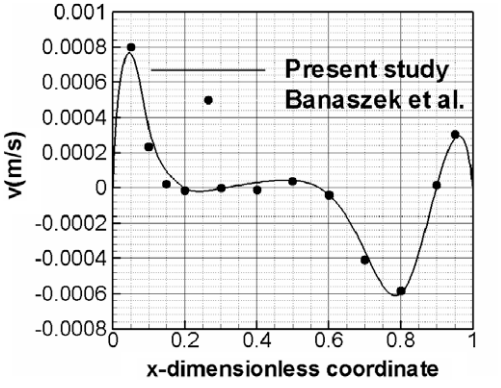

(A) Code validation

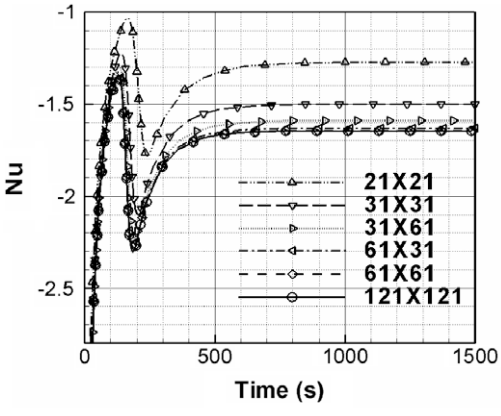

(B) Grid dependency test

Fig. 2. Mid-height vertical velocity distribution comparison of present study results with those of Banaszek et al. [14] (A) and time history of average Nusselt number computed at the bottom wall for grid dependency test with 10 °C bottom wall temperature ($Ra_T = 9.135 \times 10^3$) without solutal convection (B).

For $t \geqslant 0$, the boundary conditions are

$$\begin{aligned} &T = T_h, \;\; C = C_l; \quad y = 0, \;\; 0 \leq x \leq L, \\ &T = T_l, \;\; C = C_h; \quad y = L, \;\; 0 \leq x \leq L, \\ &\frac{\partial T}{\partial x} = \frac{\partial C}{\partial x} = 0; \quad x = 0, \;\; x = L. \end{aligned} \tag{10}$$

Fig. 1(A) shows the schematic diagram for solution domain with coordinate system and boundary conditions.

3. Numerical method

Eqs. (1)–(4) are discretized using co-located generalized coordinate system with equal space. By the relation of coordinate transformation from Cartesian coordinate system including independent variables x, y to general coordinate system including independent variables ξ, η, the generalized discretization equation can be expressed using the control volume approach [11] as follows

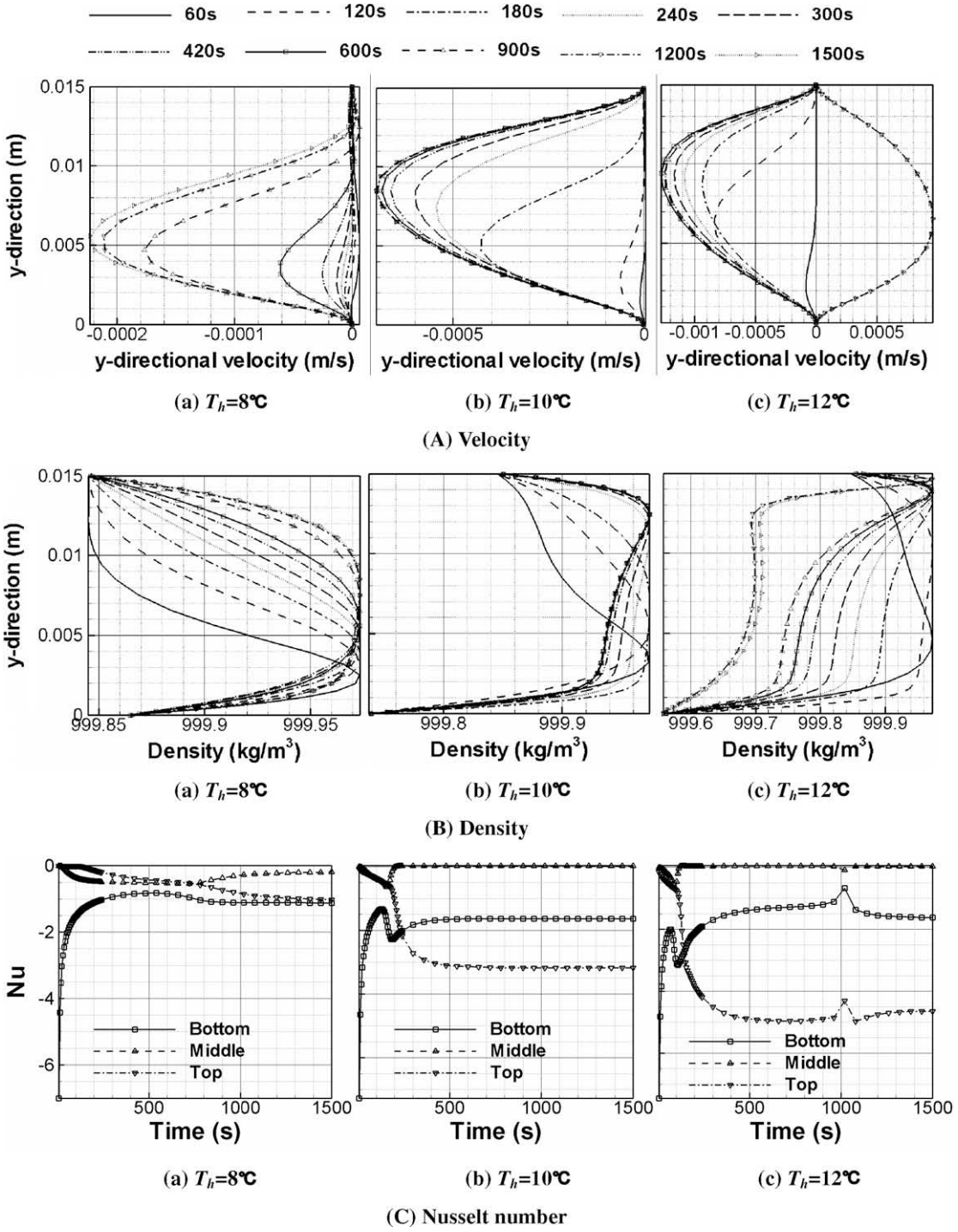

Fig. 3. Distributions of vertical velocity (A) and density (B) at the vertical center line and time history of average Nusselt number (C) at the various horizontal lines for different bottom wall temperature ((a) T_h = 8 °C ($Ra_T = -5.028 \times 10^2$), (b) T_h = 10 °C ($Ra_T = 9.135 \times 10^3$), and (c) T_h = 12 °C ($Ra_T = 1.976 \times 10^4$)) without solutal convection.

$$A_P \Phi_P = \sum A_{nbr} \Phi_{nbr} + S. \quad (11)$$

Usually the 1st order upwind scheme depends strongly on the grid size and the QUICK scheme [12] has good accuracy rather in small grid size but possesses inherent nonphysical oscillations and the convergence problems. In this study, considering the nonlinearity effects governing the double diffusive convection phenomena, it is important both robustness to converge and accuracy, therefore 2nd order upwind scheme is used. SIMPLE algorithms proposed by Patankar [11] is used to couple the momentum and continuity equations. Non-uniform collocated grid is used and pressure oscillation occurred by using collocated grid is prevented by momentum interpolation method proposed by Rhie and Chow [13]. All equations are solved by applying an implicit iterative method of line by line TDMA solver. For code validation, we conduct the numerical calculation with the same conditions of Banaszek et al. [14] and compare the present study with the result of Banaszek et al. [14] as shown in Fig. 2(A). In this figure, vertical velocity distributions agree very well with the Banaszek et al. [14]. Also, grid dependency test is done by using grid size from 21×21 to 121×121 for the case of 10 °C bottom wall temperature without solutal convection as shown in Fig. 2(B). It shows the time history of average Nusselt number at bottom wall. In this figure, it is observed that no significant difference is found at 61×31, 61×61, and 121×121 grid size. Therefore in this study, 61 horizontal and 31 vertical control volumes are used in calculations with denser grid clustering near the boundaries and vertical center line using the exponential function for the grid distribution as shown in Fig. 1(A). To ensure convergence of the numerical algorithm, the relative change of dependent variables is applied by the convergence criteria

$$\frac{\sum_{i,j=1}^{im,jm} \left| \Phi_{i,j}^{n+1} - \Phi_{i,j}^{n} \right|}{\sum_{i,j=1}^{im,jm} \left| \Phi_{i,j}^{n} \right|} < 10^{-6}, \quad (12)$$

where Φ represents a dependent variable, i.e., u, v, T, or C. Superscript n denotes previous calculation state and $n+1$ notes current calculation state in the iterative solution method and subscript i and j indicate index of grid point.

4. Results and discussion

It is expected that there is a specific relation between thermal and solutal buoyancy force which governs the thermo-solutal convection phenomena. Therefore, in order to investigate the heat, mass, and fluid flow characteristics due to buoyancy-driven force induced by thermal and solutal convection in this study, numerical calculations are carried out in a square cavity filled with water subjected to different bottom wall temperature and top wall concentration in the range $-5 \times 10^2 < Ra_T < 2 \times 10^4$ for pure water and $10^5 < Ra_S < 4 \times 10^5$, $10^6 < Ra_S < 4 \times 10^6$, and $2 \times 10^6 < Ra_S < 8 \times 10^6$ for salt water for Lewis number by 10, 100, and 200, respectively.

4.1. Effect of bottom wall temperature without solutal convection

Figs. 3 and 4 are presented to show the time history of vertical velocity, density at the vertical center line, average Nusselt number distribution at various horizontal lines and particle tracking/isotherms. From the velocity profile as shown in Fig. 3(A) it is observed that the flow occurs from the lower side with negative value of velocity and absolute velocity increases with the progress in time and increasing bottom wall temperature. The location of absolute value of maximum velocity moves upward with increasing bottom wall temperature. For 8 °C bottom wall temperature, multi-cellular flow structure is developed with time. Whereas for 10 °C bottom wall temperature, rolling flow structure is developed and for the case 12 °C bottom wall temperature pluming flow structure is developed with time as shown in Fig. 4. From the particle tracking in Fig. 4, it is found that secondary flow has developed from the bottom wall and grows up suppressing the upper cells as time progresses. The suppressed upper cells get merged into a single cell and then disappear at about 120 s whereas the lower cell grows in size to a single cell occupying half of the cavity showing typical rolling flow structure. The isotherms are almost horizontal indicating conduction is the dominant mode of heat transfer before 60 s. After 60 s, the isotherms deform to the counter clock wise direction indicating the development of convection dominant flow until 960 s. It is observed that after 1020 s, isotherms deform to the clock wise direction due to the flow inversion as shown in Fig. 4(F)–(H). Furthermore it is found that the corner cell at the left top wall grows in size suppressing lower cells as time progresses. Suppressed lower cell is divided into two cells by growing corner cell at 1020 s later. After 1080 s, the corner cell disappears and a single cell making plume flow structure occupies the entire half cavity showing typical plume flow structure. From the density profile in Fig. 3(B), maximum density region moves up-

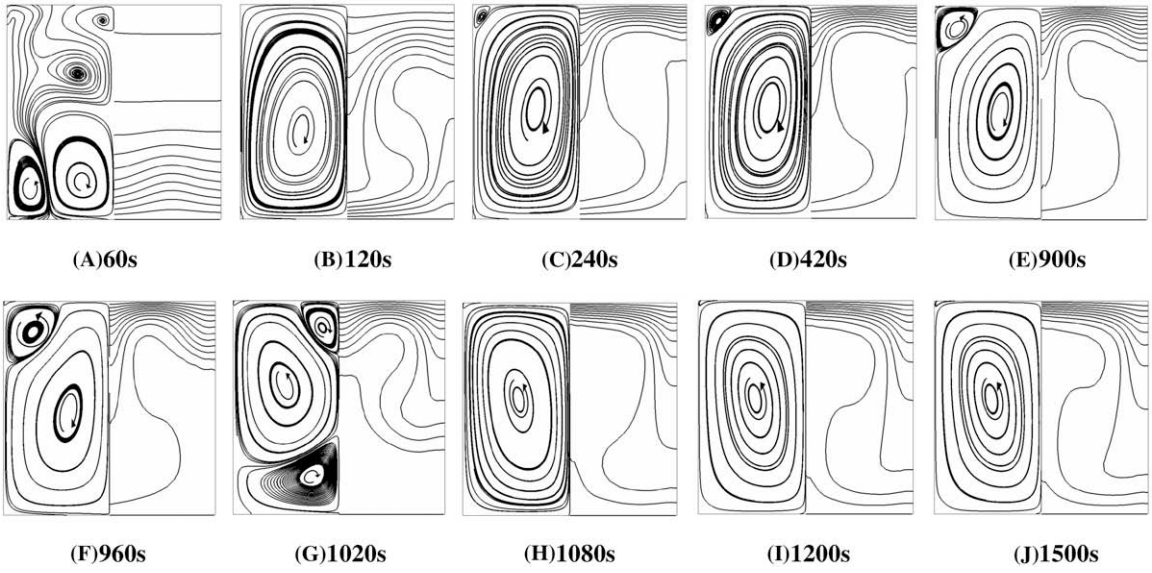

Fig. 4. Particle tracking and isotherms skipped by 1 °C as time progresses for 12 °C bottom wall temperature (T_h = 12 °C ($Ra_T = 1.976 \times 10^4$)) without solutal convection. (A) 60 s, (B)120 s, (C) 240 s, (D) 420 s, (E) 900 s, (F) 960 s, (G) 1020 s, (H) 1080 s, (I) 1200 s, and (J) 1500 s later.

ward with time and increasing bottom wall temperature. From the average Nusselt number profile shown in Fig. 3(C) negative sign of average Nusselt number indicates heat transfer direction from bottom to top. It is found that average Nusselt number at mid-height moves to zero as time progresses and increasing bottom wall temperatures as seen in Fig. 3(C)(b) and (c). Increasing bottom wall temperature increases the absolute value of average Nusselt number at the bottom and top wall. Especially, at the top wall, the increase of absolute value of average Nusselt number appears remarkably with increasing bottom wall temperature. Through the comparison of velocity (Fig. 3(A)(c)) and average Nusselt number (Fig. 3(C)(c)) it reveals that sudden peak value of average Nusselt number is developed around 1000 s due to the generation of flow inversion from rolling to plume flow structure as seen in Fig. 4.

4.2. Effect of top wall concentration and bottom wall temperature with $Le = 10$

4.2.1. Velocity and density distributions

Fig. 5 is presented to show vertical velocity profile for different values of top wall concentration and bottom wall temperature with time. For 8 °C bottom wall temperature, it is observed that the flow structure changes from rolling (Fig. 5(A)(a) and (b)) to plume (Fig. 5(A)(c)) with increasing top wall concentration as time progresses. Also, for 10 °C bottom wall temperature it is observed

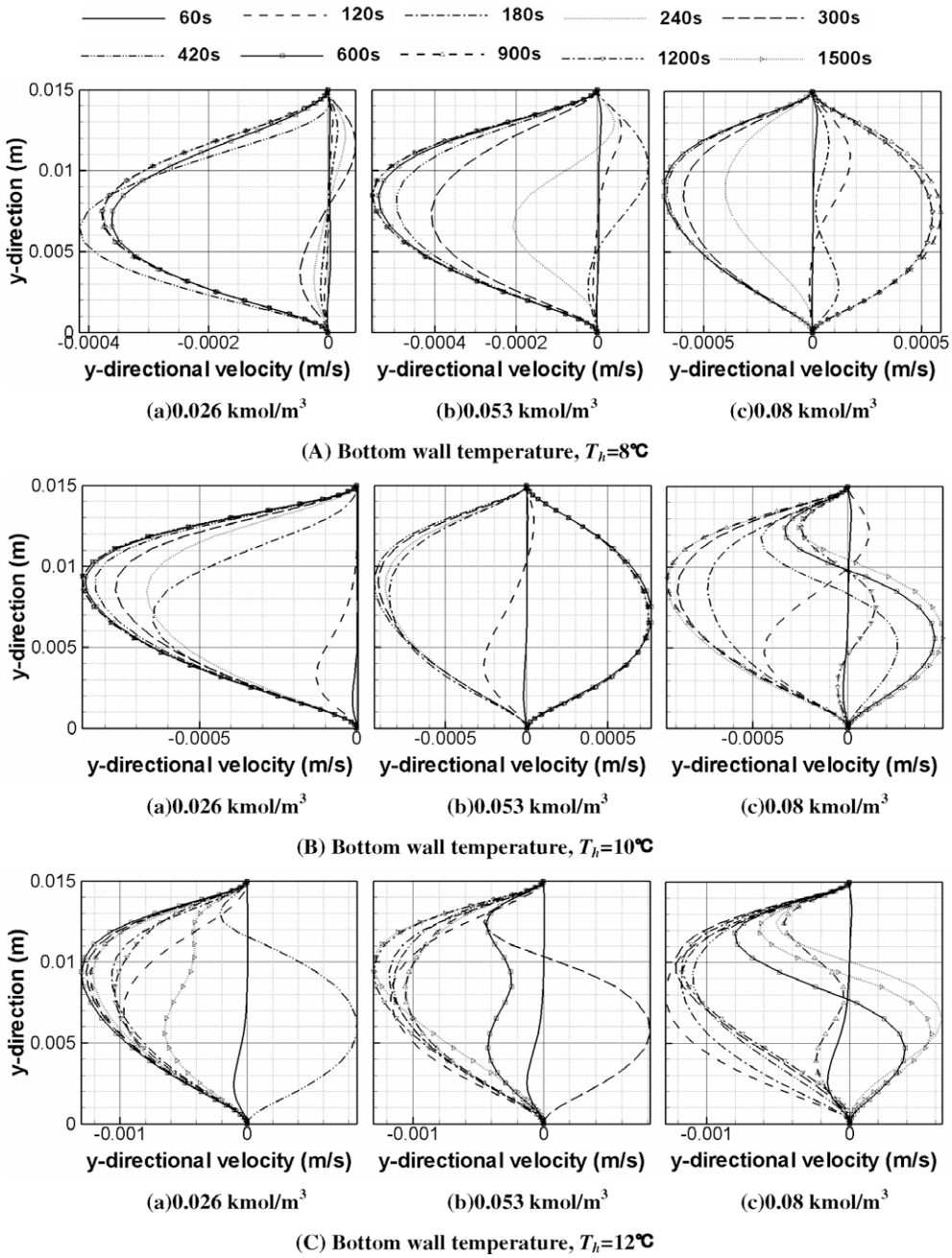

Fig. 5. Vertical velocity distributions as time progresses for different top wall concentration and bottom wall temperature ((A) T_h = 8 °C, (B) T_h = 10 °C, and (C) T_h = 12 °C) at the vertical center line at Le = 10. (a) 0.026 kmol/m^3 ($Ra_S = 1.257 \times 10^5$), (b) 0.053 kmol/m^3 ($Ra_S = 2.563 \times 10^5$), and (c) 0.08 kmol/m^3 ($Ra_S = 3.869 \times 10^5$) top wall concentration (C_h).

that as increasing top wall concentration, the flow structure changes in order of rolling (Fig. 5(B)(a)), plume (Fig. 5(B)(b)), and oscillatory two cells (Fig. 5(B)(c)) in the half of cavity as time progresses. Further increase of buoyancy force associated with an increase of bottom wall temperature leads to the change of flow structure in order of oscillatory rolling as shown in Fig. 5(C)(a) and (b) and oscillatory two cells in the half of cavity as shown in Fig. 5(C)(c) with increasing top wall concentration as time progresses. From these results, it reveals that as increasing buoyancy force associated with an increase of bottom wall temperature and top wall concentration the flow structure changes in order of rolling, plume (flow inversion), oscillatory two cells, oscillatory rolling, and oscillatory two cells as time progresses.

Fig. 6 depicts density profile for different top wall concentration and bottom wall temperature with time. In these figure, maximum density region propagates upward with the progress in time as shown in Fig. 6(A)(a), (B)(a), and (C)(a) because the rate of thermal diffusion is faster than solutal diffusion due to $Le > 1$. It is found that at the steady state, y-directional change of density is nearly zero around mid-height region of the cavity as seen in Fig. 6(A)(c) and (B)(b) indicating the onset of flow inversion from rolling to plume flow structure which corresponds to velocity dis-

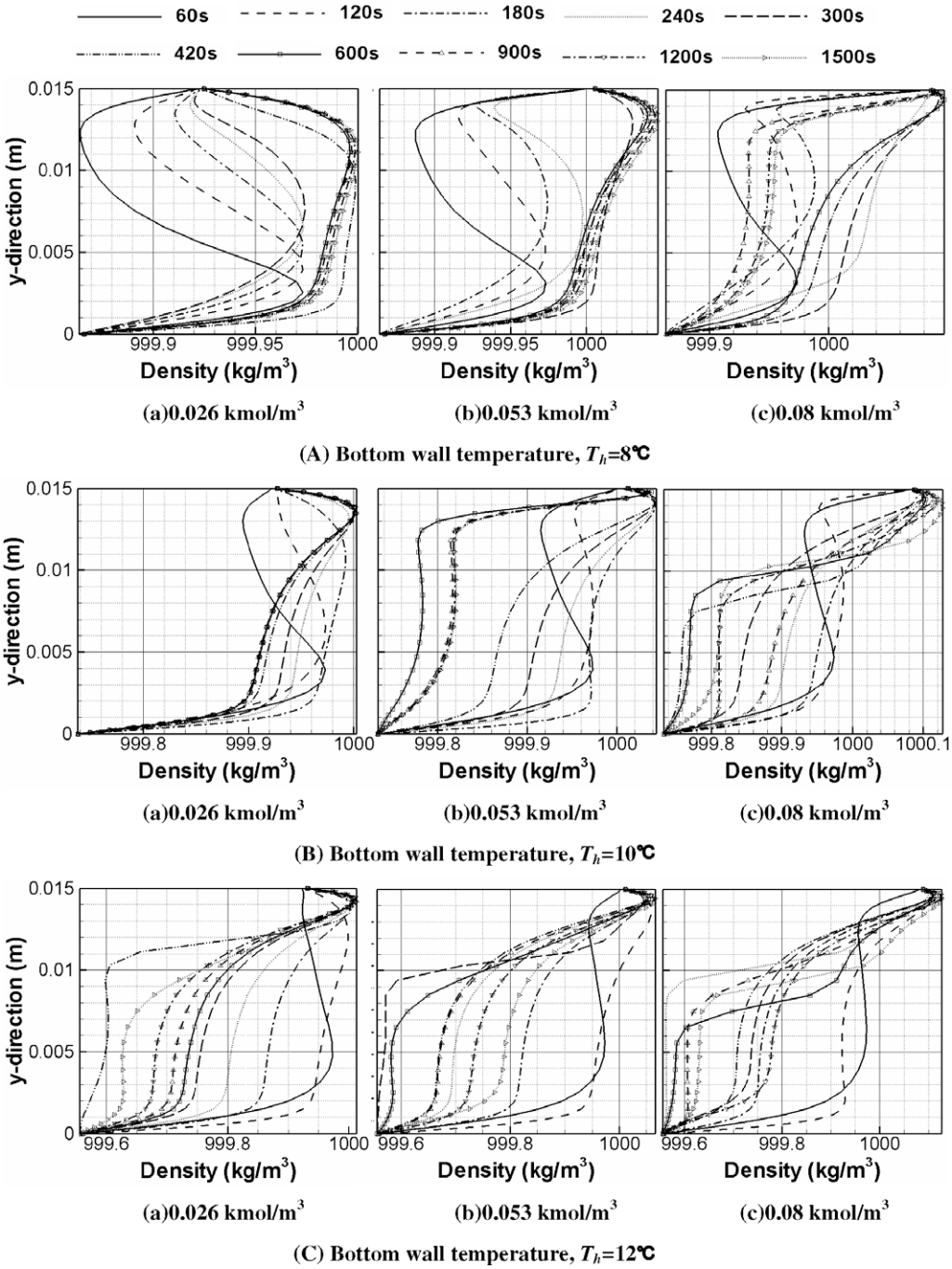

Fig. 6. Density distributions as time progresses for different top wall concentration and bottom wall temperature ((A) T_h = 8 °C, (B) T_h = 10 °C, and (C) T_h = 12 °C) at the vertical center line at Le = 10. (a) 0.026 kmol/m^3, (b) 0.053 kmol/m^3, and (c) 0.08 kmol/m^3 top wall concentration (C_h).

tribution as seen in Fig. 5(A)(c) and (B)(b). Further increase of buoyancy force results in oscillation of maximum density position with time as shown in Fig. 6(B)(c) and (C)(a)–(c).

Fig. 7 is presented to show particle tracking and isotherms with time for 8 °C and 10 °C bottom wall temperature with 0.08 kmol/m^3 top wall concentration. Since the solution domain is symmetrical about the vertical center line, particle tracking are presented in the left half of the cavity and isotherms are presented in the right half of the cavity. For 8 °C bottom wall temperature as shown in Fig. 7(A), it is found that at an earlier time, secondary flow has developed from the bottom and top wall (Fig. 7(A)(a)). Until about 60 s the flow inside the cavity is divided horizontally and the heat transfer between the cells is only by conduction since there is no exchange of particles between the cells and the predominant mode of heat transfer remains in conduction. Before 60 s, the isotherms are almost horizontal indicating conduction is the dominant mode of heat transfer. After 120 s, the flow is vertically divided and there is mixing of fluid particles from top to bottom. The convection mode of heat transfer starts in and this is also indicated by the vertical deformation of the isotherms around 120 s. A further increase in time makes the flow becoming bi-cellular and the heat transfer becoming convection dominant due to the mixing of fluid particles over the entire part of the cavity and this is also indicated by the almost vertical isotherms except at the top of the cavity as shown in Fig. 7(A)(d) and (e). After 120 s, the isotherms deform to the counter clock wise direction indicating the development of convection dominant flow until 720 s. Further increase in time introduces multi-cellular motion again making the heat transfer of conduction dominant as shown in Fig. 7(A)(h). Further increase in time makes the flow vertically divided bi-cellular and heat transfer of convection dominant one as shown in Fig. 7(A)(i) and (j). Left side cell at the upper wall grows in size suppressing the middle cells (Fig. 7(A)(b) and (c)) as time progresses. The suppressed middle cells disappear at about 240 s and left side cell grows into a single cell making rolling flow structure as seen in Fig. 7(A)(d). After 720 s as shown in Fig. 7(A)(g)–(i), it is found that the corner cell at the left top wall grows in size suppressing lower cells as time progresses. Suppressed lower cell is divided into two cells by growing

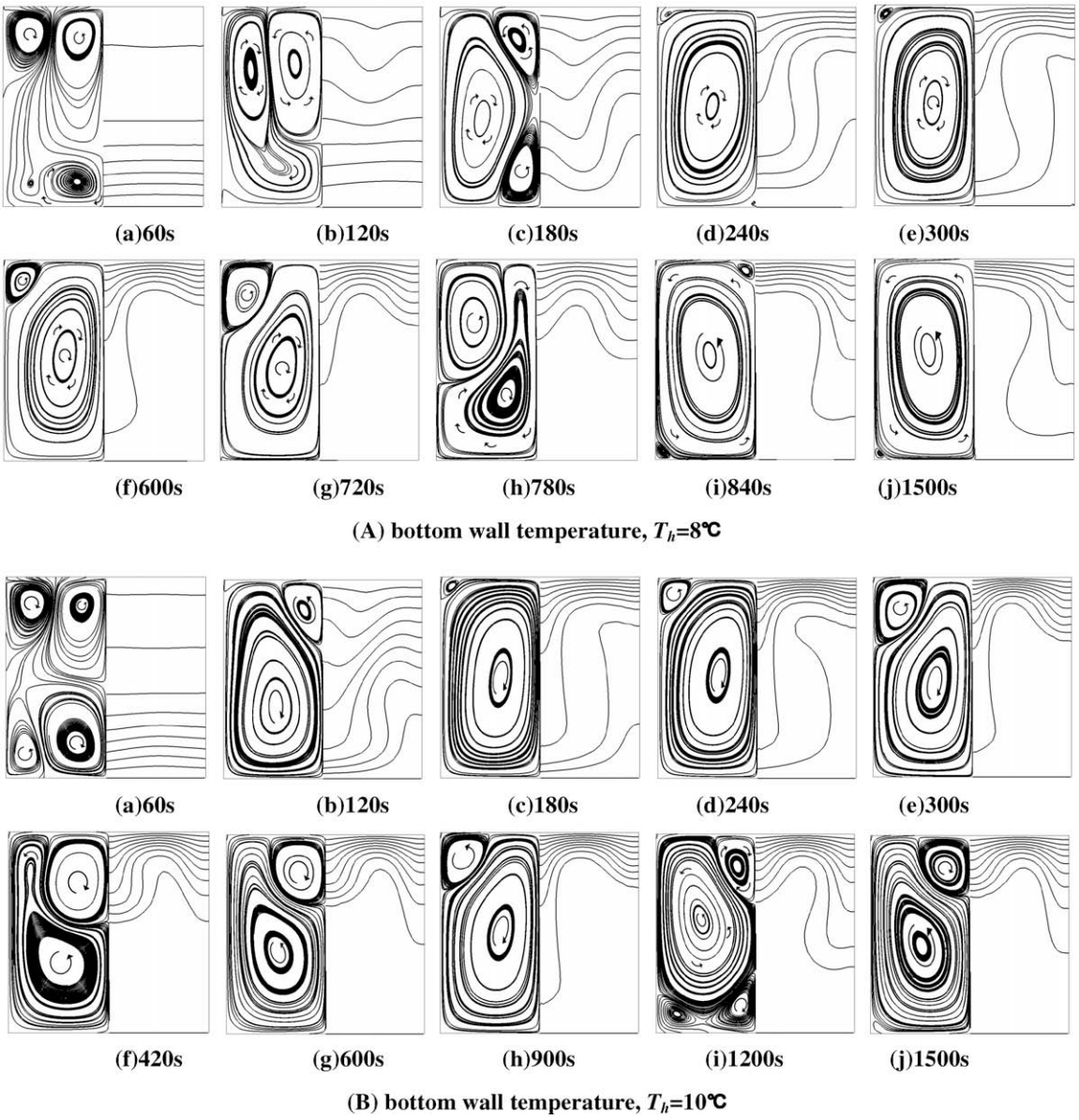

Fig. 7. Particle tracking and isotherms skipped by 1 °C as time progresses for 8 °C bottom wall temperature (A) and 10 °C bottom wall temperature (B) with 0.08 kmol/m^3 top wall concentration (C_h) at Le = 10.

corner cell at 840 s later. After 840 s, the corner cell disappears and a single cell making plume flow structure occupies the entire half cavity. This flow inversion phenomenon is confirmed by isotherms in Fig. 7(A)(f)–(j).

For 10 °C bottom wall temperature, from the particle tracking as seen in Fig. 7(B), it is found that at an earlier time, secondary flow that occurs at the bottom and top wall grows up suppressing the upper cell (Fig. 7(B)(b)) as time progresses. At 180 s later, multi cells get merged into a single cell making rolling flow structure as shown in Fig. 7(B)(c). Until 60 s, the isotherms are almost horizontal indicating conduction dominant heat transfer. After 120 s, the isotherms deform counter clock wise indicating the beginning of convection dominant heat transfer until 300 s. After that, the corner cell at the left top wall and middle cell at the top wall occur suppressing lower cell and get merged into a single cell making rolling and pluming flow structure repeatedly showing oscillatory two cells flow structure as shown in Fig. 7(B)(f)–(j).

4.2.2. Nusselt and Sherwood number distributions

Fig. 8 is presented to show average Nusselt number profile for different top wall concentration and bottom wall temperature with time. It is observed that in steady state the absolute value of average Nusselt number decreases in the bottom wall, is maintained zero at the mid-height region and increases at the top wall with increasing top wall concentration as shown in Fig. 8(A). At $t < 300$ s it is found that there are zero gradient break points at

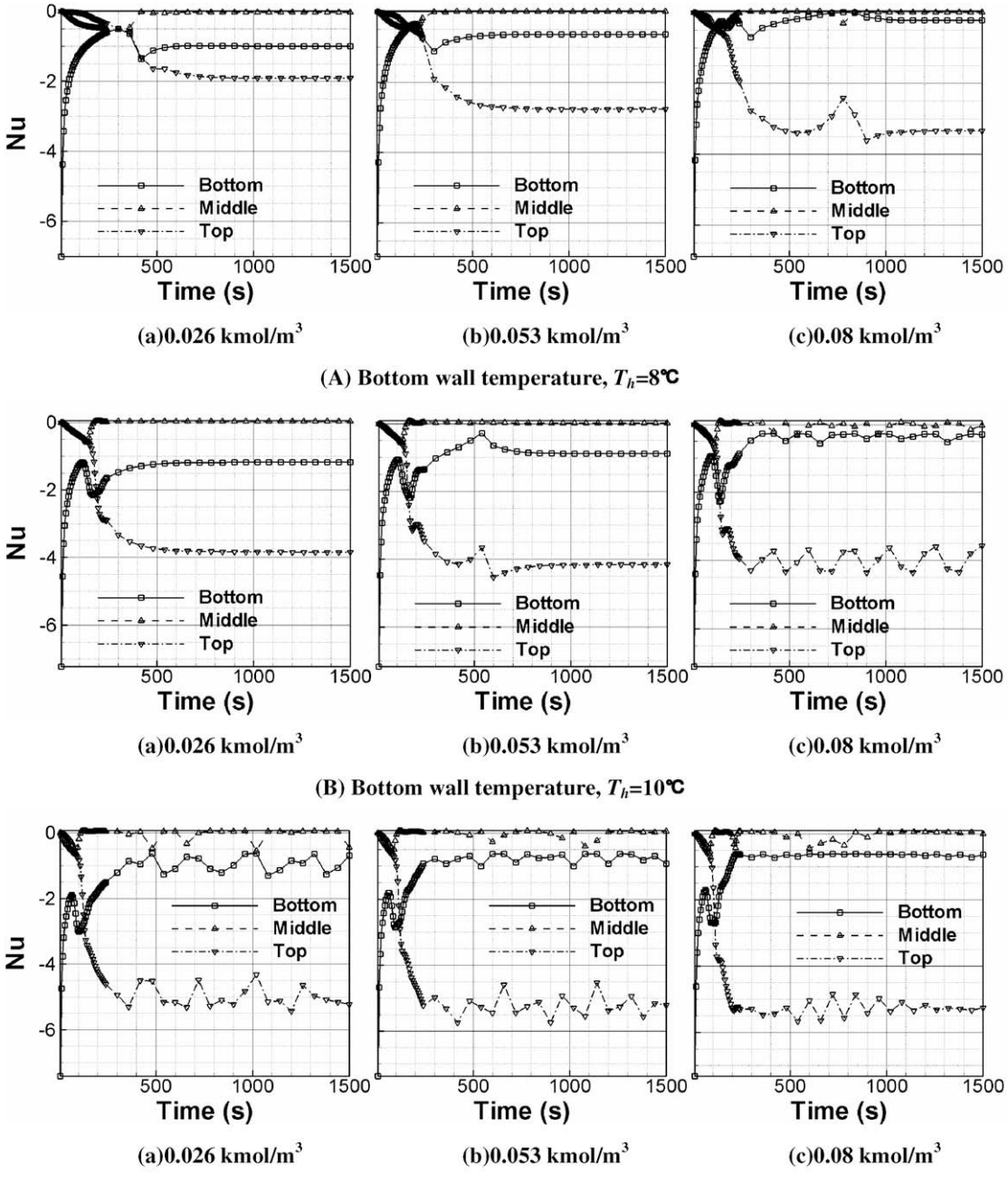

Fig. 8. Time history of average Nusselt number for different top wall concentration and bottom wall temperature ((A) T_h = 8 °C, (B) T_h = 10 °C, and (C) T_h = 12 °C) at the various horizontal line at Le = 10. (a) 0.026 kmol/m^3, (b) 0.053 kmol/m^3, and (c) 0.08 kmol/m^3 top wall concentration (C_h).

the bottom wall and mid-height region with time indicating that convection is the dominant heat transfer mode as seen in Fig. 8. In these figures, at the bottom wall, first zero gradient break point (minimum absolute value of average Nusselt number) implies conduction dominant mode of heat transfer and second zero gradient break point (maximum absolute value of average Nusselt number) implies convection dominant mode of heat transfer as seen in Fig. 8(B)(a). Because the conduction mode of heat transfer is a slow one and convection is fast mode of heat transfer, this maximum and minimum value is also clearly shown in the average Nusselt number as is seen in Fig. 3(C)(b) and more clearly in Fig. 2(B). As the steady state is reached the heat transfer is a conduction convection conjugate one. These zero gradient break points occur early and the width around zero gradient break points becomes short with increasing top wall concentration as seen in Fig. 8(A) and bottom wall temperature as seen in Fig. 8(A)(a), (B)(a), and (C)(a). Those effects do not appear clearly for 12 °C bottom wall temperature as shown in Fig. 8(C) because fully developed thermal convection is attained. It is observed that an increase in top wall concentration and bottom wall temperature leads to sudden peak value of average Nusselt number as shown in Fig. 8(A)(c) and (B)(b) which indicates inversion of flow structure from rolling to plume as shown in the corresponding velocity profile (Fig. 5(A)(c) and (B)(b)). Further increase of buoyancy force due

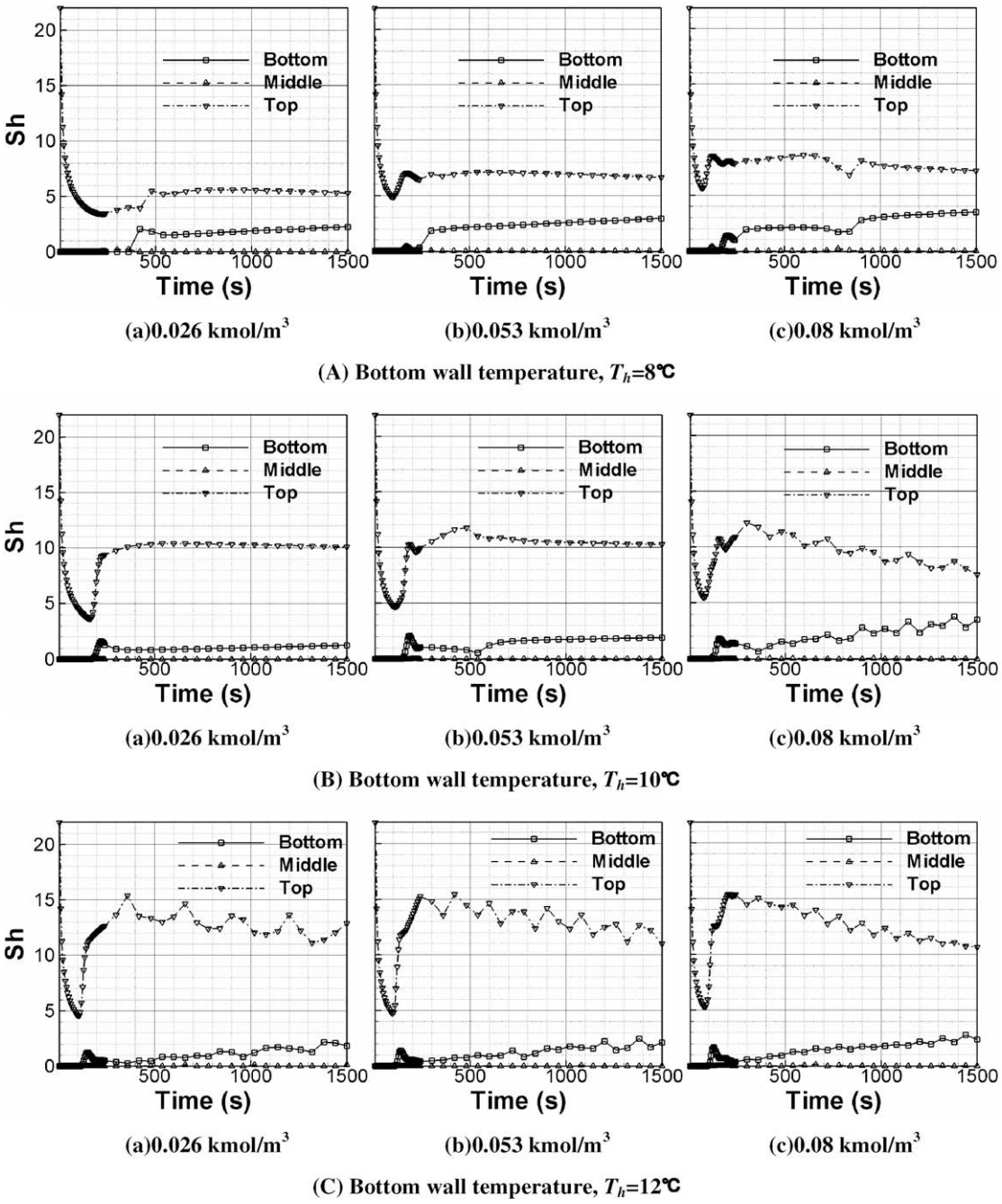

Fig. 9. Time history of average Sherwood number for different top wall concentration and bottom wall temperature ((A) T_h = 8 °C, (B) T_h = 10 °C, and (C) T_h = 12 °C) at the various horizontal line at Le = 10. (a) 0.026 kmol/m^3, (b) 0.053 kmol/m^3, and (c) 0.08 kmol/m^3 top wall concentration (C_h).

to an increase of top wall concentration and bottom wall temperature results in the oscillation of average Nusselt number as seen in Fig. 8(B)(c) and (C)(a)–(c).

Fig. 9 shows the averaged Sherwood number profile with different top wall concentration and bottom wall temperature with time. It is found that for 8 °C bottom wall temperature, the value of average Sherwood number increases at the bottom wall, is maintained zero at the mid-height region and increases at the top wall with increasing top wall concentration as shown in Fig. 9(A). It is observed further that an increase in the bottom wall temperature affects the stability of the solution which leads to the oscillatory behavior of average Sherwood number especially at the bottom and top wall as shown in Fig. 9(B)(c) and (C)(a)–(c). Also, it reveals that the cycle of oscillation becomes short at the top wall with increasing top wall concentration as seen in Fig. 9(C). These oscillations increase the time required to attain the steady state. Because of these oscillations, the 10 °C bottom wall temperature with 0.08 kmol/m^3 top wall concentration and 12 °C bottom wall

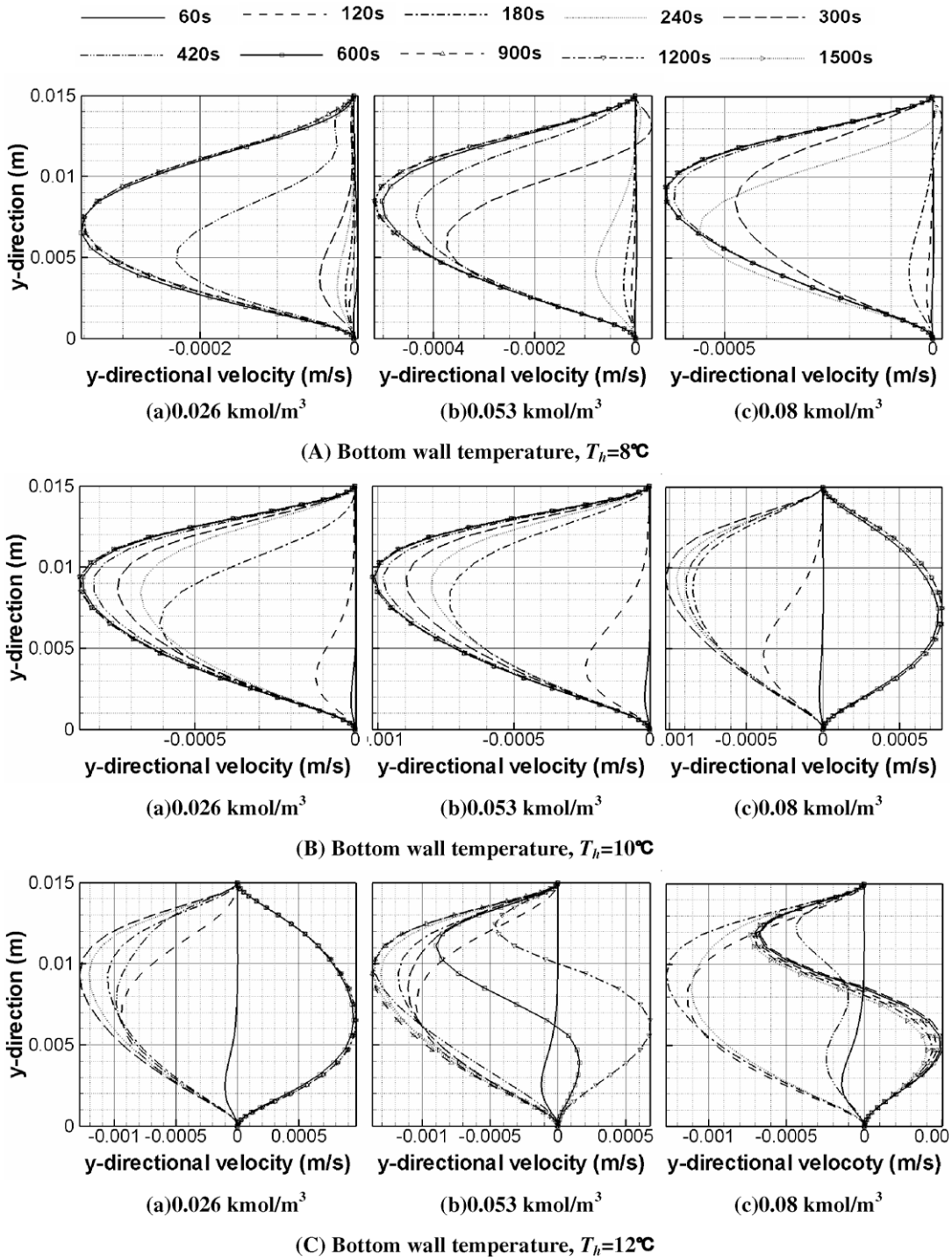

Fig. 10. Vertical velocity distributions as time progresses for different top wall concentration and bottom wall temperature ((A) T_h = 8 °C, (B) T_h = 10 °C, and (C) T_h = 12 °C) at the vertical center line at Le = 100. (a) 0.026 kmol/m^3 ($Ra_S = 1.257 \times 10^6$), (b) 0.053 kmol/m^3 ($Ra_S = 2.563 \times 10^6$), and (c) 0.08 kmol/m^3 ($Ra_S = 3.869 \times 10^6$) top wall concentration (C_h).

temperature with 0.026 kmol/m^3, 0.053 kmol/m^3, and 0.08 kmol/m^3 top wall concentration state could not attain the steady state solution until 1500 s as seen in Fig. 9(B)(c) and (C)(a)–(c).

4.3. Effect of bottom wall concentration and temperature with Le = 100

4.3.1. Velocity and density distributions

Fig. 10 shows vertical velocity distribution with different top wall concentration and bottom wall temperature as time progresses. In these figures, for 8 °C bottom wall temperature, the absolute value of velocity increases with increasing top wall concentration as time progresses. And in the steady state, the region of maximum value of velocity moves in the upward direction with increasing top wall concentration as shown in Fig. 10(A). For 10 °C bottom wall temperature, there is flow inversion from rolling to plume flow structure with increasing top wall concentration as shown in Fig. 10(B)(c). It is observed that further increase of buoyancy force leads to the change of the flow structure from plume as seen in Fig. 10(C)(a) to oscillatory two cells in the half of the cavity

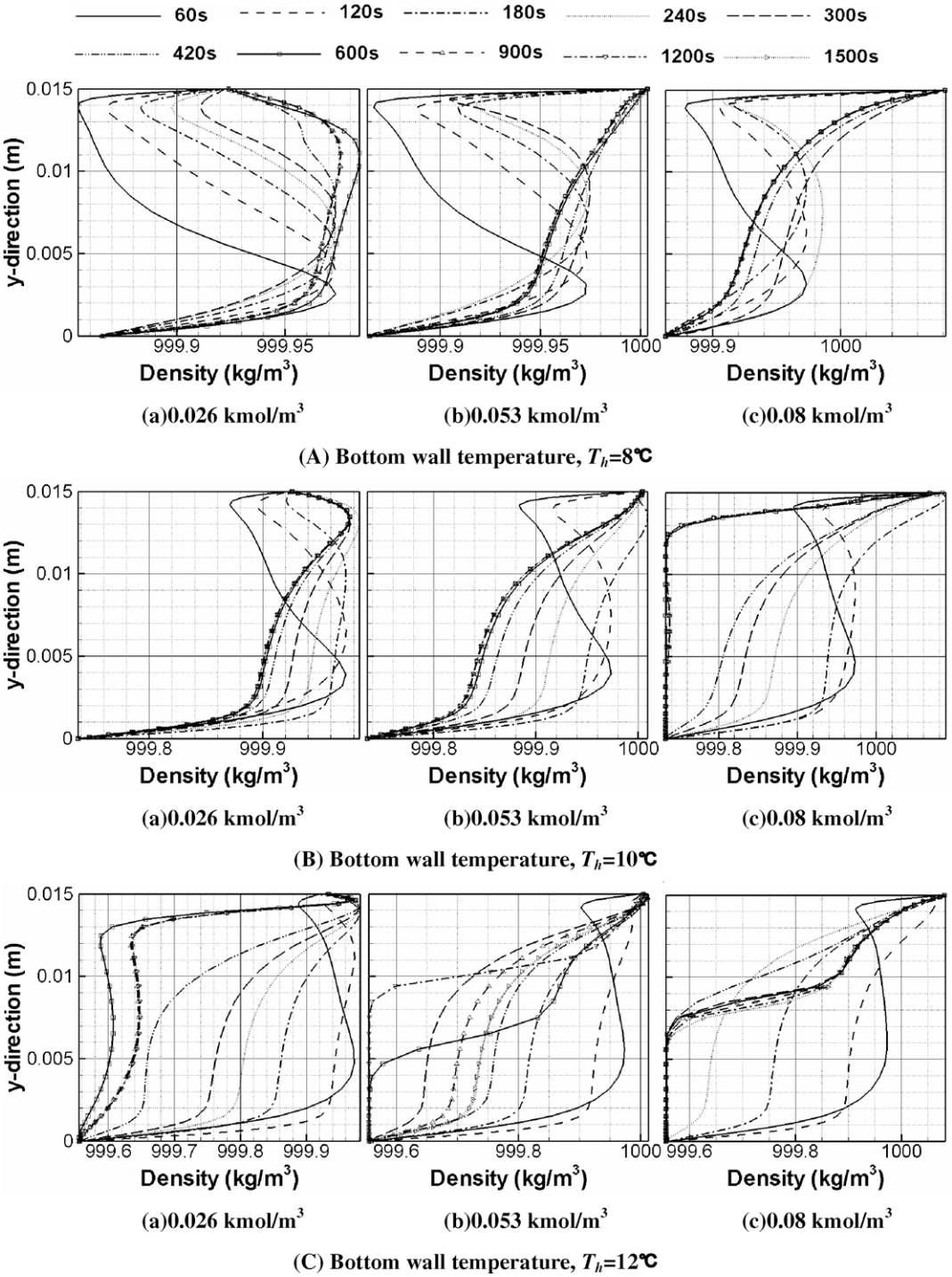

Fig. 11. Density distributions as time progresses for different top wall concentration and bottom wall temperature ((A) T_h = 8 °C, (B) T_h = 10 °C, and (C) T_h = 12 °C)) at the vertical center line at Le = 100. (a) 0.026 kmol/m^3, (b) 0.053 kmol/m^3, and (c) 0.08 kmol/m^3 top wall concentration (C_h).

as seen in Fig. 10(C)(b) and (c). From the comparison of corresponding velocity profile as seen in Fig. 5, it is found that an increase in the value of Lewis number reduces the amplitude of oscillatory flow.

Fig. 11 depicts density distribution at the vertical center line for different top wall concentration and bottom wall temperature with time. In these figures, maximum density region propagates upward with increasing bottom wall temperature as shown in Fig. 11(A)(a), (B)(a), and (C)(a) due to an increase of buoyancy force. It is found that at the steady state, y-directional change of density is nearly zero around mid-height region of the cavity as seen in Fig. 11(B)(c) and (C)(a). It is the typical phenomena which indicates the onset of flow inversion from rolling to plume flow structure which corresponds to velocity distribution as seen in Fig. 11(B)(c) and (C)(a). Further increase of buoyancy force results in the oscillation of density with time as shown in Fig. 11(C)(b) and (c). Also the density distributions do not attain to steady state.

4.3.2. Nusselt and Sherwood number distributions

Fig. 12 is presented to show average Nusselt number profile for different top wall concentration and bottom wall temperature with time. It is observed that in steady state the absolute value of average Nusselt number decreases at the bottom wall, is maintained zero at the mid-height region and increases at the top wall with increasing top wall concentration as shown in Fig. 12(A) and (B). On the other hand, the absolute value of average Nusselt number

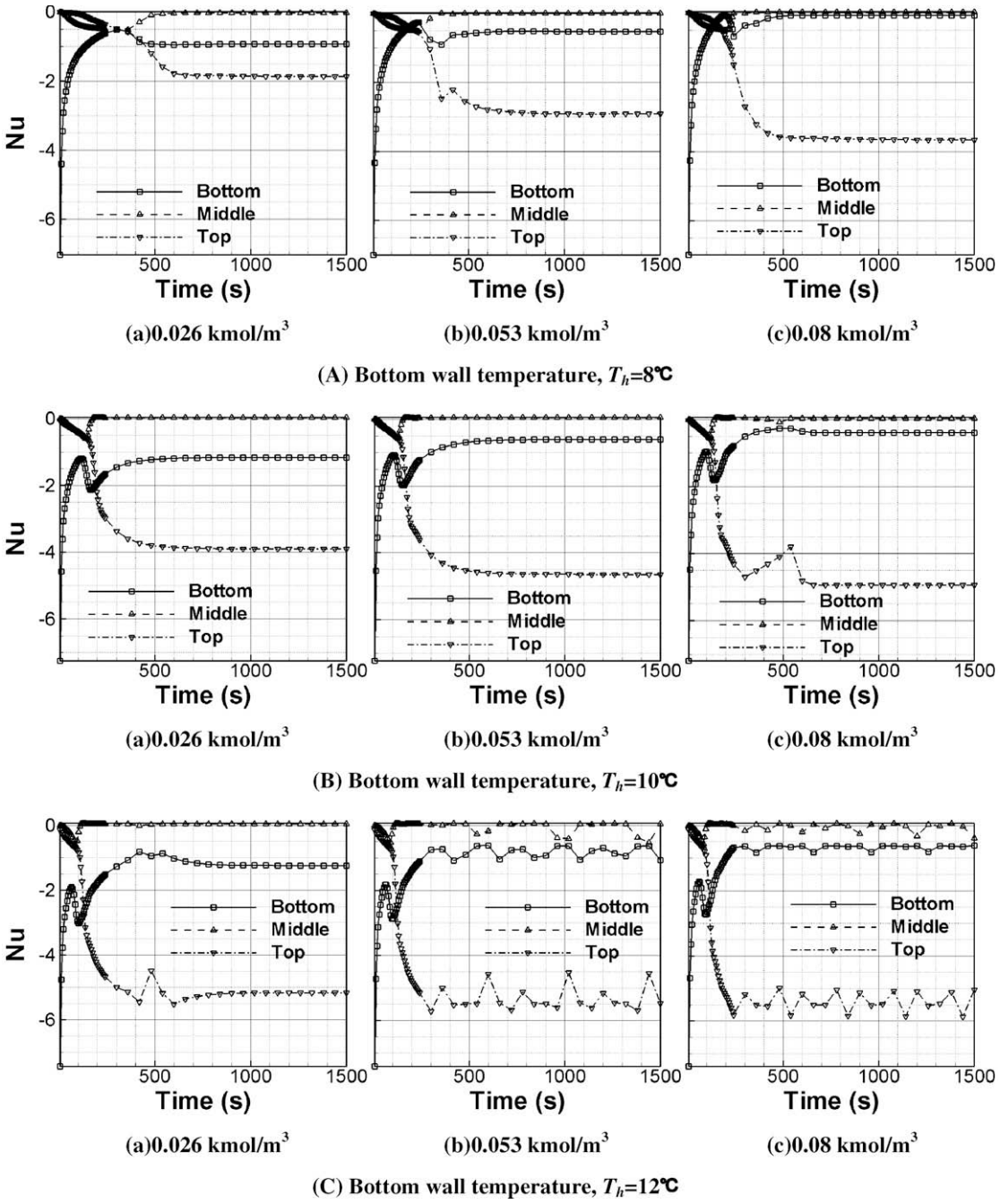

Fig. 12. Time history of average Nusselt number for different top wall concentration and bottom wall temperature ((A) T_h = 8 °C, (B) T_h = 10 °C, and (C) T_h = 12 °C) at the various horizontal line at Le = 100. (a) 0.026 kmol/m^3, (b) 0.053 kmol/m^3, and (c) 0.08 kmol/m^3 top wall concentration (C_h).

increases except at the mid-height region with increasing bottom wall temperature as shown in Fig. 12(A)(a), (B)(a), and (C)(a). At $t < 300$ s, it is observed that there are zero gradient break points at the bottom wall and mid-height region indicating that convection is the dominant heat transfer mode as seen in Fig. 12. In these figures, zero gradient break points occur early and the width around zero gradient break points decreases with increasing top wall concentration as seen in Fig. 12(A) and bottom wall temperature as seen in Fig. 12(A)(a), (B)(a), and (C)(a). It is observed that an increase in top wall concentration and bottom wall temperature leads to sudden peak value of average Nusselt number at the top wall as shown in Fig. 12(B)(c) and (C)(a) which indicates inversion of flow structure from rolling to plume as shown in the corresponding velocity profile (Fig. 10(B)(c) and (C)(a)). Further increase of buoyancy force through an increase of concentration and temperature at the top and bottom wall, respectively, results in the oscillation of average Nusselt number as seen in Fig. 12(C)(b) and (c).

Fig. 13 shows the averaged Sherwood number profile with different top wall concentration and bottom wall temperature with time. It is found that the value of average Sherwood number is maintained zero at the bottom wall and mid-height region and increases at the top wall with increasing top wall concentration and bottom wall temperature as shown in Fig. 13(A) and (A)(a), (B)(a), and (C)(a). From the comparison of corresponding average Sherwood number distribution for $Le = 10$ as seen in Fig. 9, the value

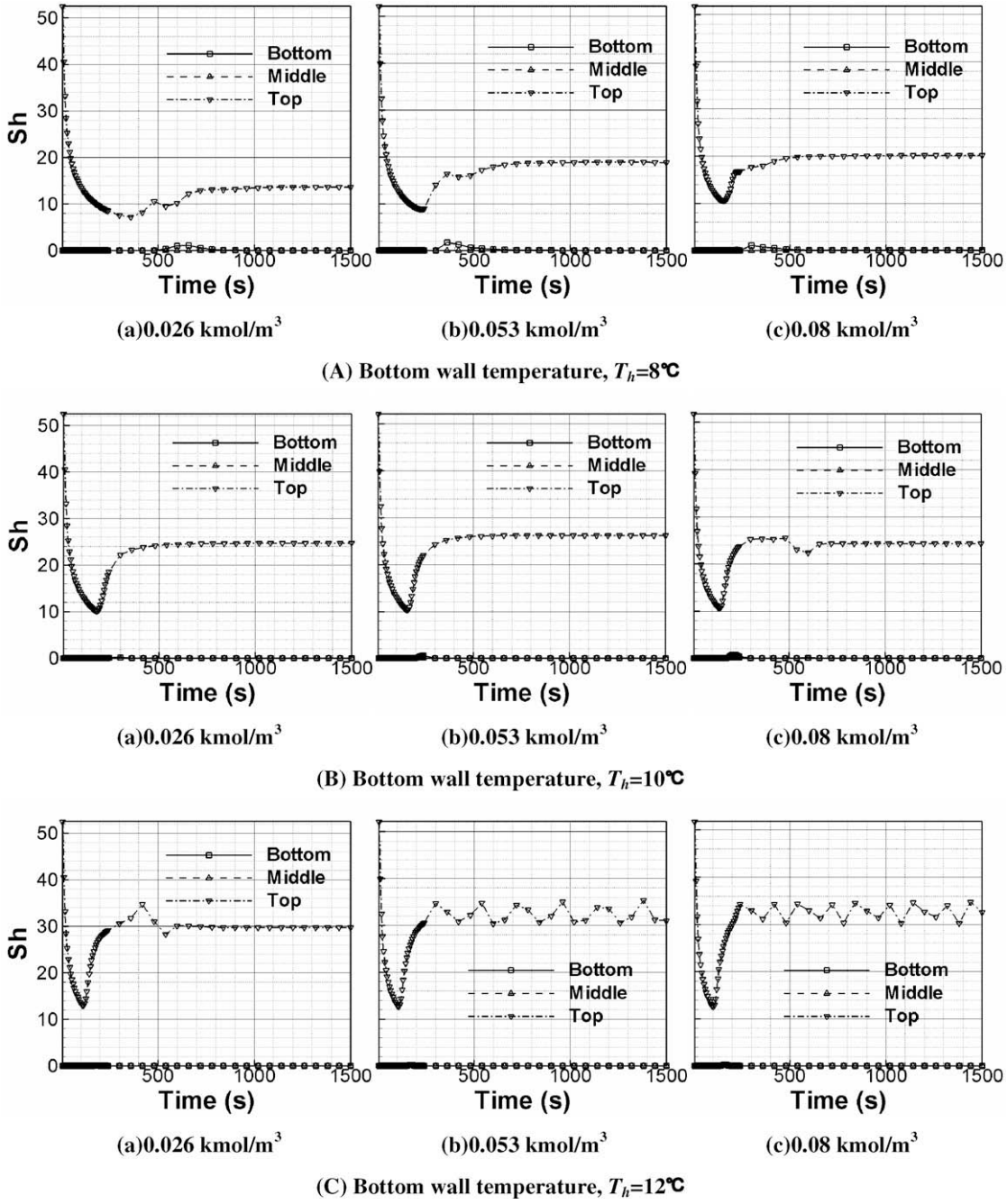

Fig. 13. Time history of average Sherwood number for different top wall concentration and bottom wall temperature ((A) $T_h = 8$ °C, (B) $T_h = 10$ °C, and (C) $T_h = 12$ °C) at the various horizontal line at $Le = 100$. (a) 0.026 kmol/m^3, (b) 0.053 kmol/m^3, and (c) 0.08 kmol/m^3 top wall concentration (C_h).

of average Sherwood number at the bottom wall decreases to zero and it reveals that an increase in the value of Lewis number slows down mass transfer due to a decrease of mass diffusivity. It is observed that further increase of top wall concentration and bottom wall temperature affects stability of the solution which leads to oscillation of average Sherwood number especially at the top wall as shown in Fig. 13(C)(b) and (c). Also, it reveals that the period of oscillation becomes short at the top wall with increasing top wall concentration as seen in Fig. 13(C)(b) and (c). These oscillation increases the time required to attain the steady state. In the present work, the case of 12 °C bottom wall temperature with 0.053 and 0.08 kmol/m^3 top wall concentration could not attain the steady state solution until 1500 s as seen in Fig. 13(C)(b) and (c).

4.4. Effect of bottom wall concentration and temperature with *Le* = 200

For the case *Le* = 200, there are no significant difference of velocity, density, average Nusselt number and Sherwood number distributions when we compare them with these of the results for *Le* = 100. For vertical velocity and density distribution at the vertical center line, flow inversion from rolling to plume flow structure occurs at the same boundary condition such as *Le* = 100 (10 °C bottom wall temperature with 0.08 kmol/m^3 top wall concentration and 12 °C bottom wall temperature with 0.026 kmol/m^3 top wall concentration) showing nearly same characteristics as mentioned in Section 4.3.1. As a results, the time history of average Nusselt number and Sherwood number show qualitatively same characteristics as mentioned at Section 4.3.2.

4.5. Effect of Lewis number

Fig. 14 depicts the average Nusselt and Sherwood number profiles of the steady state at the top wall for different bottom wall temperature and top wall concentration and critical Grashof number which classifies flow structure into two regions that correspond to rolling, plume, and oscillating two cell flow structure in half of the cavity with Lewis number. It is observed that an increase

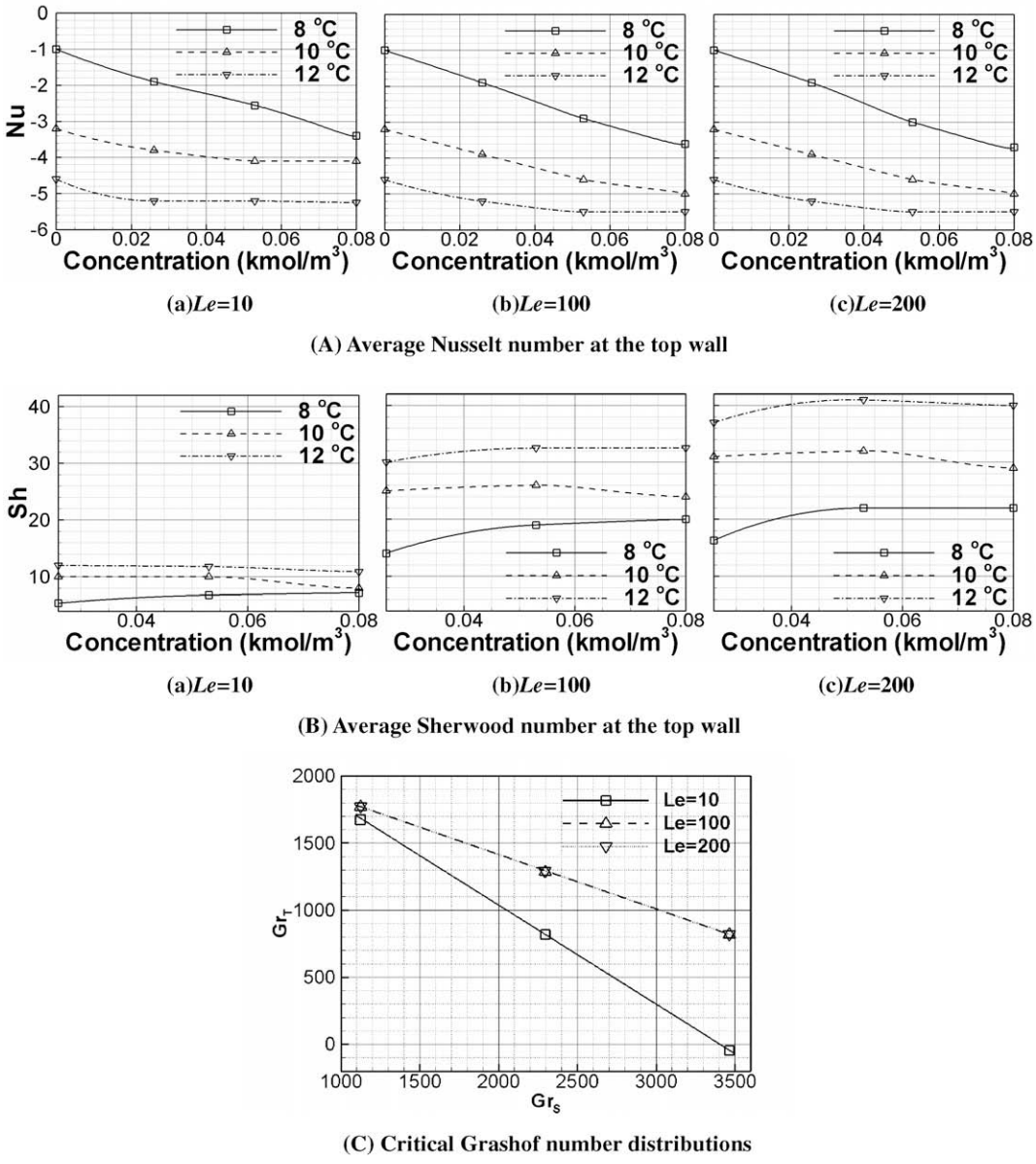

Fig. 14. Average Nusselt (A) and Sherwood (B) number distributions at the steady state in the top wall for the variation of top wall concentration and Lewis number ((a) *Le* = 10, (b) *Le* = 100, and (c) *Le* = 200) and critical Grashof number distributions with Lewis number (C).

of top wall concentration and bottom wall temperature leads to an increase of absolute value of Nusselt number at the top wall with increasing values of Lewis number due to a relative increase of thermal buoyancy force and thermal diffusivity as shown in Fig. 14(A). Further increase in Lewis number (Le = 100, 200) does not affect the absolute value of Nusselt number at the top wall as seen in Fig. 14(A)(b) and (c) because thermal convection is already in the fully developed state. Also, it is found that Sherwood number increases with an increase in Lewis number at the top wall as shown in Fig. 14(B) because an increase of Lewis number implies decrease of mass diffusivity which results in higher difference of y-directional concentration distribution at the top wall. For 10 °C and 12 °C bottom wall temperature, Sherwood number no longer increases with increasing top wall concentration where top wall concentration is greater than 0.053 kmol/m^3 due to the change of flow structure from rolling to plume and oscillating two cells. In Fig. 14(C), upper side of each curve indicates flow region having plume and oscillating two cell flow structure and lower side indicates flow region with rolling flow structure. It is found that an increase in the value of Lewis number increases the range of critical Grashof number resulting in the expansion of flow region with rolling flow structure. On the other hand, a decrease in Lewis number leads to an increase in the range of critical Grashof number that develops plume and oscillating two cell flow structure as seen in Fig. 14(C).

5. Conclusion

The effects of density maximum in water on heat and mass transfer in a square cavity have been studied for various values of bottom wall temperature and top wall concentration with Lewis number. It is observed that the nonlinearity of density including maximum value of zero gradient break point leaves strong effects on the heat and mass transfer due to the formation of rolling or plume flow structure and multi-cellular fluid flow. The nonlinear behavior of heat transfer rate results due to the presence of double diffusive convection including maximum density effect acting as an insulated obstacle. The typical patterns of velocity, density, Nusselt, and Sherwood number which classify the dominant mode of transfer process are studied. It reveals that the typical order of magnitude in absolute value of average Nusselt number is in turn of bottom, mid-height, and top for diffusion dominant transfer whereas top, bottom, and mid-height for convection dominant transfer. The results show that at the top wall, a higher convective heat transfer can be achieved by increasing Lewis number and species Grashof number. The results indicate that there is a temporal maximum absolute value of average Nusselt and Sherwood number followed by a temporal minimum absolute value of average Nusselt and Sherwood number in a small time interval ($0 < t < 300$ s) and the steady state is reached after a certain time interval at the bottom wall. These time intervals are reduced with increasing Lewis number. Further the critical Grashof number which accounts for oscillatory heat and mass transfer in each Lewis number is studied and it reveals that an increase in Lewis number results in slowing down oscillation and oscillation cycle becomes shorter with an increase of top wall concentration.

References

[1] S.L. Goren, On free convection in water at 4 °C, Chem. Eng. Sci. 21 (1966) 515–518.
[2] L. Robillard, P. Vasseur, Convective response of mass of water near 4 °C to a constant cooling rate applied on its boundaries, J. Fluid Mech. 118 (1982) 123–141.
[3] L. Robillard, P. Vasseur, Transient natural convection heat transfer of water with maximum density effect and supercooling, ASME J. Heat Transfer 103 (1981) 528–534.
[4] K.R. Blake, D. Poulikakos, A. Bejan, Natural convection near 4 °C in a horizontal water layer heated from bellow, Phys. Fluids 27 (11) (1984) 2608–2616.
[5] S. Chandrasekhar, Hydrodynamics and Hydromagnetic Stability, Dover, New York, 1981, pp. 9–219.
[6] P.G. Drazin, W.H. Reid, Hydrodynamics Stability, Cambridge U. P., Cambridge, England, 1981, pp. 32–63.
[7] J. Lee, M.T. Hyun, Y.S. Kang, Confined natural convection due to later heating in a stably stratified solution, Int. J. Heat Mass Transfer 33 (5) (1990) 869–875.
[8] J. Lee, M.T. Hyun, J.H. Moh, Numerical experiments on natural convection in a stably stratified fluid due to side wall heating, Numer. Heat Transfer A 18 (1990) 343–355.
[9] J.W. Lee, J.M. Hyun, Time-dependent double diffusion in a stably stratified fluid under lateral heating, Int. J. Heat Mass Transfer 34 (1991) 2409–2421.
[10] P. Kandaswamy, S. Sivasankaran, N. Nithyadevi, Buoyancy-driven convection of water near its density maximum with partially active vertical walls, Int. J. Heat Mass Transfer 50 (2007) 942–948.
[11] S.V. Patankar, Numerical Heat Transfer and Fluid Flow, Hemisphere, McGraw-Hill, New York, 1980, pp. 30–40, 67–68, 90–100.
[12] B.P. Leonard, A stable and accurate convective modeling procedure based on quadratic upstream interpolation, Comput. Methods Appl. Mech. Eng. 19 (1979) 59–68.
[13] C.M. Rhie, W.L. Chow, Numerical study of the turbulent flow past an airfoil with trailing edge separation, AIAA J. 21 (11) (1983) 1525–1532.
[14] J. Banaszek, Y. Jaluria, T.A. Kowalewzki, M. Rebow, Semi-implicit FEM analysis of natural convection in freezing water, Numer. Heat Transfer A 36 (1999) 449–472.